Additive Manufacturing 98 (2025) 104645

Contents lists available at ScienceDirect

Additive Manufacturing

journal homepage: www.elsevier.com/locate/addma

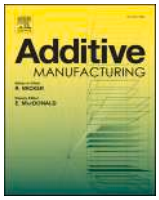

3D ice lithography and post-processing using gold organometallic precursor

Bingdong Chang [a,1], Gwendoline A.E. Anand [a,1], Hoa Thanh Le [a,c], Xiyuan Liu [a], Thomas W. Hansen [b], Jose María de Teresa [d], Anpan Han [a,*]

[a] Department of Civil and Mechanical Engineering, Technical University of Denmark, Kongens-Lyngby 2800, Denmark
[b] DTU Nanolab, Technical University of Denmark, Kongens-Lyngby 2800, Denmark
[c] Lotus Microsystems, Hvidovre 2650, Denmark
[d] Instituto de Nanociencia y Materiales de Aragón (INMA), CSIC-Universidad de Zaragoza, Zaragoza 50009, Spain

ARTICLE INFO

Keywords:
$Au(acac)Me_2$
Thermosets
Gold nanoparticles

ABSTRACT

3D ice lithography (3DIL) is an emerging method for fabricating polymeric 3D objects with submicrometer patterns. However, there are no studies on 3DIL using metal-containing precursors. In addition, unlike numerous post-processing studies of two-photon polymerization (2PP) and focused electron beam-induced deposition (FEBID), there are no 3DIL post-processing investigations. Here, we present a 3DIL process using an organometallic precursor (gold dimethyl acetylacetonate, $Au(acac)Me_2$), and its first post-processing study. We investigated 3D processing parameters and post-processing using Ar-, air annealing, and O_2 plasma. X-ray photoelectron spectroscopy (XPS), atomic force microscopy, energy-dispersive X-ray spectroscopy, and transmission electron microscopy were used for materials analysis. Our results show (i) 3DIL processed materials exhibit thermoset properties, as they decompose rather than melt at elevated temperatures; (ii) free metal atoms diffuse and form clusters, here, gold nanoparticles with a diameter of around 10 nm were formed; (iii) oxygen treatments remove carbon-based ligands while leaving noble metals behind. Also, Ar annealing leads to less material loss than air annealing, while O_2 plasma generates oxidized Au states and efficiently removes carbon ligands. Ar annealing at 600 °C reduces the carbon XPS signals significantly and increases the gold XPS signal by ten times, giving a good purification effect but with a high material removal of around 95 %. We printed large Au metalorganic 3D structures (>1000 times larger volume than FEBID), which suggests 3DIL bridges the gap between the capabilities of 2PP and FEBID. The unique capabilities of organometallic compounds to detect environmental changes can position 3DIL for sensing applications, and 3DIL is a safe and non-toxic technique to manufacture nanoparticle-containing 3D structures, which may have applications in many fields such as nanophotonics, drug delivery, and catalysis.

1. Introduction

Technological advances require the development of micro- and nanoscale components with smaller sizes, higher precision, and 3D features. This is essential in fields such as electronics [1,2], optics [3,4], microfluidics [5,6], and communication [7,8]. Two-photon polymerization (2PP), focused electron beam-induced deposition (FEBID), focused ion beam-induced deposition (FIBID), and 3D ice lithography (3DIL) are complementary additive manufacturing (AM) technologies that fabricate complex 3D objects at the submicrometer scale. Each method offers unique resolution, materials, and throughput advantages. 2PP relies on the nonlinear absorption of two photons to induce the polymerization of patterns smaller than 100 nanometers [9]. Its starting materials (precursors) are acrylate or silane-based photopolymers [10,11], with the noteworthy emergence of bio-cross-linking materials [12,13]. This technique produces intricate polymer and composite devices for optical, photonics, communications, and healthcare applications [14–16]. In FEBID and FIBID, an electron or ion beam dissociates a vaporized precursor adsorbed onto the substrate surface. Its wide range of materials includes precursors developed for chemical vapor deposition (CVD) [17]. These metalorganic precursors contain carbonyl, halogen, or alkyl compounds [18]. FEBID/FIBID allows the single-step growth of composite materials with applications as metal contacts [19,20] and fine probe tips [21,22], in superconductivity [23,24], in

* Corresponding author.
E-mail address: anph@dtu.dk (A. Han).
[1] both authors contributed equally

https://doi.org/10.1016/j.addma.2025.104645
Received 29 August 2024; Received in revised form 16 December 2024; Accepted 7 January 2025
Available online 9 January 2025
2214-8604/© 2025 The Author(s). Published by Elsevier B.V. This is an open access article under the CC BY license (http://creativecommons.org/licenses/by/4.0/).

magnetism [25,26], in photonics [27,28], as structural elements [29], etc. Fundamentally different from 2PP and FEBID is 3DIL. 3DIL is a layer-by-layer additive process involving freezing layers of a gasified precursor over the substrate surface and then patterning the obtained ice layers using an electron beam [30]. As a recently reported novel technology, 3DIL does not fit into any ISO/ASTM 52900 standard categories. It shows similarities with vat photopolymerization-based processes as it relies on cross-linking to form 3D objects, but it uses an electron beam rather than a light source, doesn't require a vat, and isn't limited to photosensitive materials. It also shares some key features of directed energy deposition, as focused electron beams deliver energy required for cross-linking of precursors. We demonstrated microfluidics and nanophotonic applications using 3DIL [30]. It can create features as small as 4 nm [31].

Post-processing methods enhance materials and device properties. Since these three AM approaches are distinct, the suitable post-processing techniques and their specific benefits vary: using thermal processes or hydrogel infusion, polymeric 2PP devices can be converted to metal oxides, which are shrunk to achieve a higher resolution [32], and metals [33,34], while FEBID materials can be purified through thermal annealing [35,36], plasma or gas treatments [37,38], electron or ion beam curing [39,40], increasing their metal content. However, post-processing of 3DIL-printed objects has not yet been investigated, and since 3DIL is fundamentally different from 2PP and FEBID, the methodology, mechanism, and potential haven't been addressed in other studies. Here we aim to address this research gap systematically by examining the effects of three post-processing techniques—air annealing, Ar annealing, and O_2 plasma—on 3DIL materials and structures. We have three hypotheses:

i. Oxygen at elevated temperatures and O_2 plasma will remove 3DIL materials because the ligands are carbon-based. Metals that do not react with O_2 will remain.
ii. Energetic electrons cross-linked organic molecules that form polymer-like structures, and since cross-linked polymers are thermosets, we hypothesize that 3DIL materials are also thermosets.
iii. Free metal atoms will diffuse and form clusters in 3DIL parts, while most ligands are cross-linked and not mobile. Thus, maintaining the original 3D structure.

We used an Au-containing organometallic compound to test our hypotheses: gold dimethyl acetylacetonate (Au(acac)Me_2). It is an excellent candidate because we do not anticipate Au will react with O_2, and the acetylacetonate ligands will likely cross-link. We determined the optimal IL parameters through Monte Carlo simulations, dose tests, and fabrication of 3D structures. Energy-dispersive X-ray spectroscopy (EDS) mapping examined the elemental composition. We studied the effect of post-processing methods (air annealing, Ar annealing, and O_2 plasma) on 2D thin films using X-ray photoelectron spectroscopy (XPS) and atomic force microscopy (AFM). We investigated post-processing parameters on 3D-printed objects using scanning electron microscopy (SEM) and EDS. Finally, we employed transmission electron microscopy (TEM) to investigate Au mobility. This work builds on our previous effort in 3D printing low-toxicity materials. In our latest paper, we investigated nonane as a starting material and showed a proof-of-concept print using the chosen gold organometallic precursor. Here, we continue this story by presenting the first systematic study of 3DIL using an organometallic precursor, including the post-processing investigation of 3DIL patterned materials and 3D structures.

2. Materials and methods

2.1. Materials

The gold organometallic precursor is gold dimethyl acetylacetonate (Au(acac)Me_2) from ABCR GmbH and was stored inside a freezer at around −15 °C. The precursor decomposes in elevated temperatures, and when exposed to air, humidity, and light. Therefore, special caution must be considered during the process. Compared to other toxic gold precursors (like Au(PF_3)Cl, and the fluorinated derivatives Au(tfac)Me_2 and Au(hfac)Me_2), there are no associated health risks or safety concerns according to its material safety data sheet (MSDS). Although there are no standardized processes for Au(acac)Me_2 precursor, we performed sample preparation, transport, and testing based on ISO/ASTM standards, and Table S1 is given in Supplementary Materials listing all the standardized methods.

2.2. 3DIL processes

We performed Monte Carlo simulations to determine optimal manufacturing parameters using CASINO v2.5. We downloaded the Benchy model from Benchy.com and sliced it using UltiMaker Cura. The 3DIL process occurs in a modified FlexSEM 1000 (Hitachi High-Tech) using a custom 3D printing program. This software can control our in-built gas injection system (GIS) and processes to generate patterns. During the printing, the sample stage was cooled down with liquid nitrogen and stored in a tank connected directly to the stage. Beam conditioning was performed each time according to the ASTM E986–04 standards to achieve the optimal beam shape for 3DIL. We invite the reader to learn more about our 3DIL setup and process here [30,41].

Before the 3DIL processes, we transferred the solid-state precursors into a glass vial inside a glovebox filled with Ar gas. The glass vial was cleaned thoroughly with acetone, ethanol, and distilled water. Then, the clean glass vial was stored in a vacuum environment inside load-lock for 1 h to eliminate any possible contaminations before being loaded into the glovebox. After precursor transfer, the filled glass vial was sealed with aluminum foil to avoid light exposure during transportation. The sealed glass vial was placed in a box with ice bags to maintain a relatively cold temperature and installed onto the SEM system. The glass vials were cleaned thoroughly, and the precursors were preserved according to the ASTM D3694–96 standard. It usually takes 1 h before the temperature of the glass vial slowly ramps up to around 20 °C. To inject the precursor into the SEM chamber, we heated the glass vial to 25 °C with a resistive heater, and we applied thermal grease to reduce thermal resistance between the glass vial and the heater. A thermocouple was attached at the bottom of the glass vial, which measured the temperature of precursors. Overheating at 30 °C could already decompose the precursors and deteriorate printing results. Therefore, precise temperature control is crucial and can be achieved by tuning PID controller settings. The solid-state precursor could then evaporate and be injected through a leak valve. A pressure gauge is used to monitor the pressure inside our GIS, which is used to estimate the thickness of organometallic ice being deposited.

To prolong the shelf-life of the precursor inside the glass vial and, at the same time, have a good resolution of 3D objects, we chose 5 kV and 10 mC/cm^2 for the electron-beam acceleration voltage and the dose, which can give a layer thickness of around 300 nm. For the 3DIL process of tall structures, a large number of layers will be expected; this could cause some practical issues, like the focus depth of the electron beam can limit the structure fidelity, and the positioning error of the stage can also be amplified. We also observed a varied layer thickness between different batches of experiments, which could be caused by the unstable precursor properties. Thus, calibration must be performed for optimized 3DIL results.

For purposes of 3DIL and post-processing, we used small pristine silicon chips as substrates. For electrical characterizations, we used silicon chips deposited with 6 μm thick silicon dioxide as insulating layers, and the silicon dioxide was grown by a wet thermal oxidation process, with processing temperature of 1075 °C and pressure of 1 bar. The chips were cleaved manually and have a size of around 1 cm by 1 cm. The corner position of the chips was used as alignment marks during

precursor deposition and exposure at different layers. In this paper, we present three letters, four 200 × 300 μm^2 thin-films, and ten Benchys. To establish a reproducible and reliable process, we fabricated more samples with different designs and substrates, which are listed in Table S2 with more details.

2.3. Characterization

A Zeiss Supra system was used for SEM imaging, and a high acceleration voltage of 15 ~ 20 kV was used for high-quality images without charging effects. The sample preparation and size characterization were performed based on the standardized ASTM E986–04. Surface morphology was characterized by an AFM ICON PT system (Bruker). XPS spectrum was obtained by XPS Nexsa (Thermo Fisher Scientific), which is equipped with monochromatic Al K-alpha photons at 1486.6 eV. A large pattern area was created for XPS measurement, and a single exposure was performed with an area dose of 5 mC/cm^2 and a beam current of 500 pA. A relatively small acceleration voltage of 5 kV was used, so the printing process can be accomplished in around 1 h 40 min, giving a thickness of around 155 nm and root-mean-square roughness R_{rms} of 13.2 nm. Pass energy was 10 eV for all measurements. The pressure of analysis chamber was around 6 × 10^{-8} mbar, the step size of spectrum was 0.1 eV and dwell time was 50 ms. Avantage data system (Thermo Fisher Scientific Inc) was used for XPS data processing, a linear background was assumed to fit the peaks on spectra with Gaussian functions. Adventitious carbon signals were used as a reference for analysis and fitting. The sample preparation, spectrum collection, and data analysis were performed based on the standardized ASTM E2735–15.

EDS measurements were performed with a detector by Oxford Instruments. The working distance was around 7 mm, and 15 eV acceleration voltage was applied to achieve characteristic signals from Au_M, while the signals from Au_Lα was not detectable. We performed EDS measurements according to the ASTM E1508–12 standard. For TEM measurements, we created ice patterns on grids with Si_3N_4 windows, and the ice structures were inspected under a Titan E-Cell 80–300ST system (FEI) with an acceleration voltage of 300 kV. Electrical properties were measured with a probe station EPS150Triax, where sheet resistance was measured with both 2-wire and 4-wire modes. We also compared electric resistance measurements with a microRSP-M300 system (Capres A/S) with a micro 4-point probe setup.

2.4. Post-processes

Plasma treatment was performed with a Tepla plasma ashing system (PVA TePla America, Inc.). Samples were placed in a barrel-type microwave plasma ashing system with an O_2 gas flow of 200 sccm, generator power of 200 W, and pressure of 1.28 bar; the total processing time was 6 min, during which the chamber temperature increased from room temperature to 84 °C. Thermal annealing was performed in an STA 449 C Jupiter Thermo-microbalance system (Netzsch-Gerätebau GmbH), where chips were placed in a ceramic crucible in an Ar or air atmosphere with a pressure of 1 bar. The system has a relatively small furnace size and has good temperature uniformity. The heat treatment setup is aligned with ISO 11358 standards. Before annealing, the furnace was preconditioned by O_2 gas at 1000 °C to remove possible carbon contaminations. Temperature was set to 250 °C for Ar and air for comparison and annealed in 10 min (temperature ramping rate was set to be 10 °C/min). Due to the small size of 3D objects, the weight change due to post-processing is below the thermogravimetric resolution of 1 μg.

3. Results and discussions

3.1. 3DIL processing and parameters optimization using gold dimethyl acetylacetonate (AuDA) precursor

The 3DIL process, shown in Fig. 1a, occurred within a customized IL instrument based on an SEM [42]. We cooled the substrates to cryogenic temperatures (~ 80 K) with liquid nitrogen. We vaporized and injected organometallic precursors into the system. The injection occurred through a needle-shaped nozzle using our gas injection system (GIS) and resulted in a disc-shaped deposition area of 5 mm in diameter. We then focused the electron beam on the deposited organometallic ice, cross-linking the material. A custom program, which we developed to assist the 3D lithography process [30], reads the G-code from a sliced 3D model, and monitors the printing process. When the procedure finished, we heated the substrate at a rate of 1 K/s to room temperature. During the thawing, the unexposed material sublimated, leaving behind the 3D objects on the substrate. We retrieved the substrates from the ice lithography system for characterization and post-processing.

To determine the most suitable 3DIL parameters, we assessed the dimensions of the basic geometric unit or voxel. The voxels approximate the interaction volumes between the primary electrons (PE) and the frozen precursor. The diameter of the voxel must be slightly larger than the target linewidth, as adjacent voxels are stitched together to form larger areas in each layer. Similarly, their height should be slightly larger than the deposited ice thickness to cross-link adjacent layers. The voxel size is estimated by Monte Carlo simulations, which statistically study the trajectory of incident electrons inside the irradiated material.

We simulated PE energies of 3 kV, 5 kV, and 7 kV to choose the optimum acceleration voltage (Fig. 1b). The estimated voxel heights are 236 nm, 550 nm, and 792 nm, with corresponding voxel diameters of 180 nm, 404 nm, and 670 nm for PE energies of 3 kV, 5 kV, and 7 kV, respectively. As expected, higher PE energy leads to larger voxels. We then compared the simulated voxel heights with the measured thickness of cross-linked organometallic ice (Fig. 1c). The cross-linked material was created by exposing an ice layer with a thickness of at least 3.2 μm, measured with AFM, to PE energies ranging from 1.5 kV to 10 kV. The simulations and experiments fit well for low PE energies; however, the deviation is significant for higher PE energies. This presents a trade-off: we can print high-resolution structures with low PE energy or achieve high throughput with higher PE energy. We selected 5 kV for the PE energy to have a high resolution while keeping a decent throughput. We then quantified the deposition rate of the ice by measuring its thickness when exposed to a PE energy of 10 kV with different injection times. The ice thickness and the injection time are linearly related, and the rate is 225 nm/min (Fig. 1d).

In addition to selecting PE energy and measuring the ice deposition rate, we needed to determine the optimum dose [30,43]. Here, we patterned squares of 5 μm by 5 μm with area doses from 1 mC/cm^2 to 100 mC/cm^2 and measured the cross-linked AuDA thickness using optical profilometry. Dose test results for PE energies of 3 kV and 10 kV are in Fig. 1e. A higher dose increases thickness until it saturates above a critical dose. Fig. 1f displays the cross-linked ice thicknesses obtained at different PE energies relative to doses. It indicates that thicker cross-linked patterns can be achieved, but a larger critical dose is necessary. However, overexposure should be avoided in 3DIL processes since the horizontal dimensions of the patterns can be stretched, deteriorating the pattern fidelity. Besides, increased surface roughness and bubbling can also be observed for higher doses. Both phenomena reduce the adhesion between different layers and damage the quality of 3D objects [30]. Therefore, we selected a dose of 10 mC/cm^2 for 5 keV PE.

After determining the optimal PE energy and dose, we verified the presence of Au (Au_M signal at 2.120 keV) and C through EDS (Fig. 1g). However, quantifying the proportion of elements is challenging due to the precursor's carbon content and the substrate's Si signals.

Finally, to validate the optimized parameters and demonstrate the

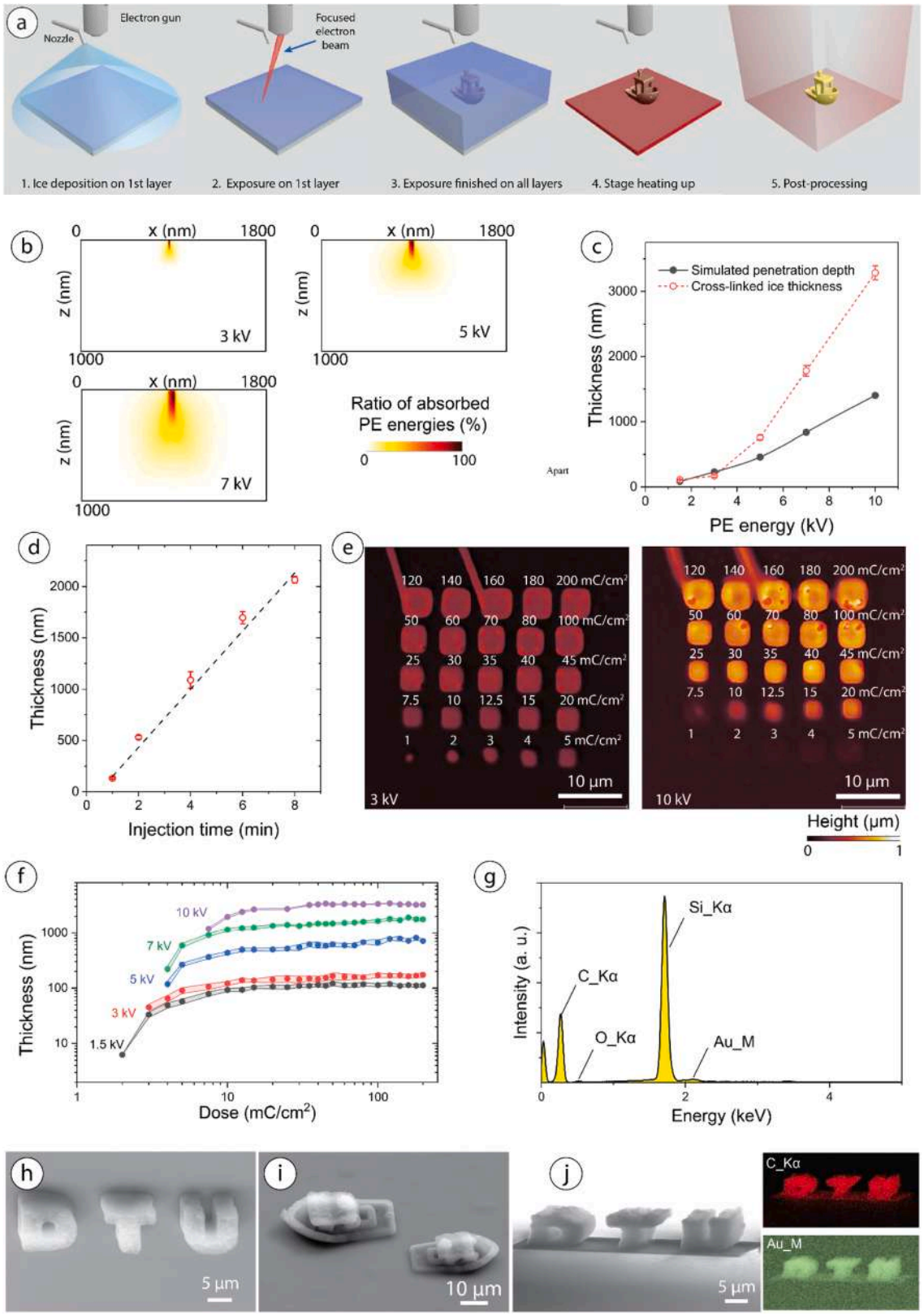

Fig. 1. (a) Process flow of 3DIL with organometallic precursors. (b) Monte Carlo simulations showing the interaction volumes of PE in Au(acac)Me_2 ice. (c) Comparison between simulated voxel height and measured thickness of cross-linked ice at different PE energies. (d) The thickness of deposited ice with injection times. (e) Dose test with PE energies of 3 kV and 10 kV, showing squares written with different doses. (f) Dose curves with PE energies of 1.5 kV, 3 kV, 5 kV, 7 kV, and 10 kV. (g) EDS spectrum of a single square pattern showing e.g. Au. SEM pictures of (h) horizontally placed "DTU" characters, (i) two Benchy boat structures, and (j) upstanding "DTU" characters, with EDS mapping, showing C and Au elements.

capabilities of 3DIL, we printed 3D objects and analyzed them with EDS to assess the elemental distribution of C and Au. Fig. 1h shows 4.7-μm-thick "DTU" characters lying horizontally on a Si substrate. Fig. 1i displays Benchy boat structures, well-known 3D models for AM process control. The boats' lengths are 40.4 μm and 31.3 μm, and their heights are 14.3 μm and 10.7 μm, respectively. The 3D features (tilted sidewalls, suspended structures) demonstrate excellent shape fidelity. Fig. 1j displays upstanding 7.2-microns-thick "DTU" characters, with well-defined hanging and suspended structures on the "T" and "D". EDS mapping revealed a uniform distribution of C and Au elements throughout the as-printed "DTU" structures. These 3D objects verify the success of the parameter optimization and the capability of 3DIL to print organometallic microstructures with excellent shape qualities.

Compared with our previous work based on nonane, 3DIL processing of Au(acac)Me_2 yields a smaller voxel depth and hence a thinner layer thickness (Table 1). This is in line with our expectations because the larger Au atoms in AuDA interact more strongly with electrons than lighter elements. AuDA 3DIL requires a lower dose and exhibits a higher throughput than nonane 3DIL, at the same acceleration voltage. These results imply that other organometallic materials might require a lower dose than alkane compounds and achieve a higher resolution. Despite using the same AuDa precursor, comparing our findings to FEBID is challenging because the FEBID dose (3 orders of magnitudes larger than 3DIL) depends on the type of geometries desired, planar or pillar, and the target metal content [44]. FEBID processing of ethylene [45], an organic compound, for instance, occurred at a higher dose than Me_2-Au-tfac in one study [46] and at a lower dose in another [44].

3DIL and FEBID can achieve feature sizes as small as 4 nm [31], and 5 nm [47], respectively. However, with a printing speed up to a thousand times faster than FEBID [48], 3DIL is more efficient for creating larger structures, as discussed in the following paragraph. Moreover, while FEBID relies on post-processing and post-grows [49,50], 3DIL does not require post-processing treatments. FEBID is therefore well-suited for fabricating nanoscale devices, whereas 3DIL is more effective for manufacturing larger, submicrometer-scale, objects.

Comparing print dimensions, 2PP offers devices up to the millimeter scale [51]. Unfortunately, it is limited to photopolymer materials and composites with low functional material concentration [52]. E.g. the maximum weight percent (wt%) of Au depends on the resin composition and varies from 0.01 wt% to 1 wt% [52]. FEBID Au-containing structures are much smaller than 2PP. E.g. Au pillars are 100 nm in diameter and 2.2-μm-tall pillars, and 50-nm-thick thin films are 20 μm x 5.0 μm [53–55]. This corresponds to volumes of $1.7 \bullet 10^{-2}$ μm^3 and 5.0 μm^3, respectively. In this study, 3D Benchy boats were 40.4-μm-long and 14.3-μm-tall. In addition, we patterned 155-nm-thick thin films that measure 200 μm x 300 μm, corresponding to a volume of 9300 μm^3. Thus, 3DIL is an effective method for producing submicrometer structures using pure organometallic precursors, which is impossible with 2PP. The 3DIL printing rate using AuDa is much faster than FEBID, and below we investigated the printed materials and post-processing.

Table 1
Comparison of 3DIL and FEBID printing parameters for organic and organometallic precursors.

Method	Precursor	Acceleration voltage [kV]	Voxel depth [nm]	Critical area dose [mC/cm^2]
3DIL	Nonane	3	420	5
3DIL	Nonane	5	600	12.5
3DIL	Au(acac)Me_2	3	240	4
3DIL	Au(acac)Me_2	5	480	8
FEBID [45]	Ethylene	2	-	$5.7 \bullet 10^3$
FEBID [46]	Me_2-Au-tfac	3	-	$3.2 \bullet 10^3$
FEBID [44]	Me_2-Au-tfac	3	-	10^4 - $2.3 \bullet 10^4$

3.2. Post-processing of e-beam cross-linked organometallic thin-films

To study the influence of post-processing methods on 3DIL and test hypothesis 1, we performed thermal annealing and oxygen-based plasma treatment, as demonstrated for FEBID [56] and 2PP [57,58]. We analyzed the as-printed and post-processed materials using XPS for chemical composition and AFM for step height and surface roughness. For XPS and AFM analysis we needed to pattern larger organometallic ice thin-films (200 × 300 μm^2) on Si chips, which have a root mean square surface roughness (R_{rms}) of less than 0.3 nm. We obtained cross-linked AuDa thin films with a layer thickness of 155 nm and surface roughness of 13.2 nm.

Fig. 2a shows the surface-sensitive XPS spectra of Au4f peaks, where the $Au4f_{7/2}$ peak at a binding energy (BE) of 83.9 eV and the $Au4f_{5/2}$ peak at 87.6 eV, both characteristic of metallic Au signals [59]. After annealing in air and Ar at 250 °C, Au4f signals increased significantly. This is due to enhanced Au contents on the surface of organometallic ice, as annealing removed carbon. O_2 plasma post-processing (max 84 °C, see methods for details) resulted in oxidized Au4f signals at around 86.3 eV ($Au4f_{7/2}^{+3}$) and 90.0 eV ($Au4f_{5/2}^{+3}$). The oxidized Au4f peaks are typically found in gold nanoparticles (AuNPs) where Au cations are bonded to oxygen [60,61]. They are caused by bonding between Au, scarcely distributed in the thin film, and high-density O radicals, generated in the plasma chamber. Fig. 2b shows the C1s signals with BE at 284.7 eV. O_2 plasma reduces the C content tremendously, while air and Ar annealing increase the intensity of the "tail" with BE between 286 eV and 290 eV, which are oxidized states of C. The increased C "tail" for Ar annealing is due to the air exposure, which leads to the oxidation of carbon atoms with dangling bonds. All three post-processing methods lead to material losses, indicated by a much smaller layer thickness of 10 nm (air annealing), 17 nm (Ar annealing), and 15 nm (O_2 plasma). This corresponds to around 90 % loss compared with the initial thickness of 155 nm. Post-processing reduces surface roughness, as shown in Fig. 2c as we measured the R_{rms} in a 1 μm by 1 μm area to be 2.1 nm (air annealing), 2.5 nm (Ar annealing), and 2.4 nm (O_2 plasma). This corresponds to around 80 % reduction compared with the initial R_{rms} of 13.2 nm.

We did additional annealing studies using argon gas because air annealing leads to significant material loss, and O_2 plasma treatment generates oxidized Au states and material loss. We used three different parameter combinations in the annealing process: 450 °C for 10 min, 450 °C for 30 min, and 600 °C for 10 min. Optical microscopy examined the morphology of patterns after post-processing (Fig. 3a**)**. Post-processing at 450 °C for 10 min resulted in an observable metallic color on the pattern surface. However, we did not observe the "shiny" metallic color with a longer annealing time of 30 min, and the pattern was hardly observable with a higher annealing temperature of 600 °C (indicated by the white box in the figure). We also used AFM to characterize the patterns after annealing, and the layer thickness was measured in an area of 1 μm by 1 μm to be 20 nm, 17 nm, and 8 nm, with R_{rms} of 2.1 nm, 1.6 nm, and 0.8 nm, respectively. This corresponds to a 90 % material loss compared with the initial thickness of 155 nm. It is also equivalent to around 90 % of R_{rms} reduction compared with the initial R_{rms} of 13.2 nm. XPS Au4f peaks, shown in Fig. 3b, show low Au peaks for the thin-film processed at 450 °C for 10 min but display a significantly increased peak intensity either by a longer annealing time or a higher annealing temperature. C1s signals, compared in Fig. 3c, suggest that C concentration is not reduced when annealed at 450 °C, however, 600 °C can reduce the signals of both C peak at BE of 284.7 eV and the "tail" of oxidized C states. Ar annealing at 600 °C achieves a high purification effect for Au but produces severe material removal (around 95 %).

These findings support our first hypothesis: oxygen at elevated temperatures and O_2 plasma remove 3DIL the cross-linked carbon-based ligands, but the non-reactive Au remains.

Comparing IL to FEBID and 2PP, there are similarities and

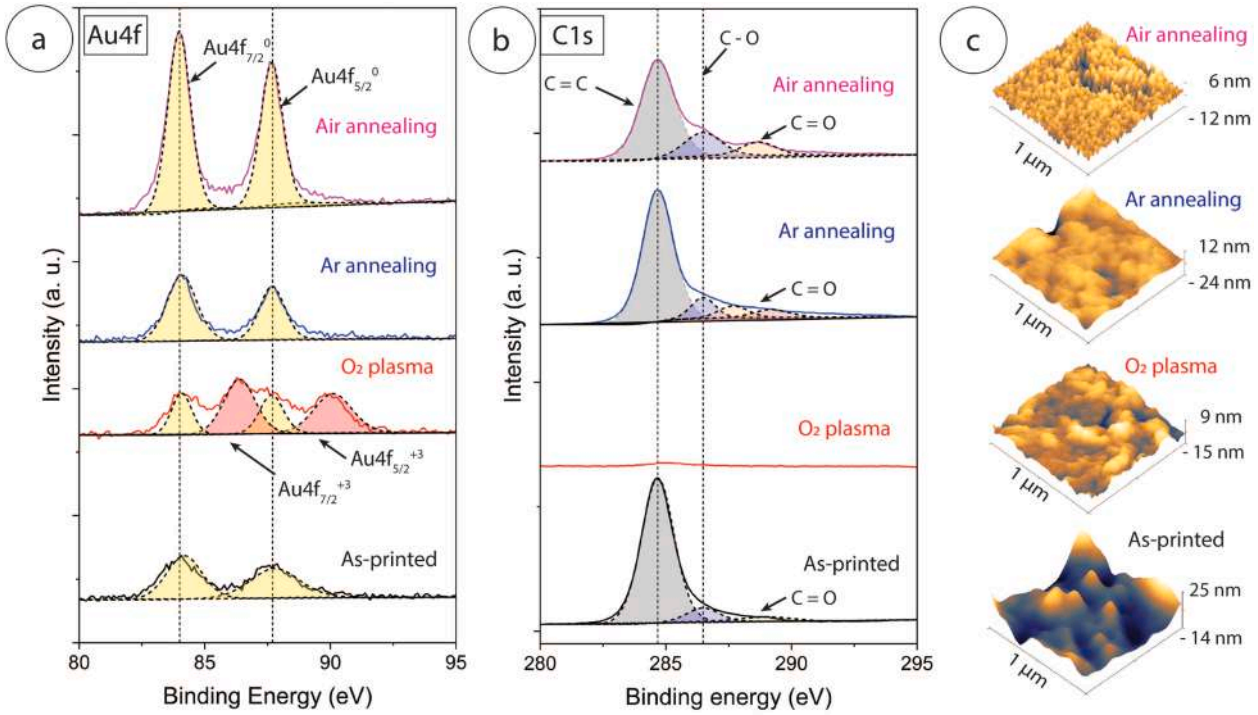

Fig. 2. XPS spectra of organometallic ice patterns as-printed and with different post-processing techniques. (a) Au4f and (b) C1s signals are compared directly. Surface roughness is also characterized on the surface of patterns, which is compared in (c).

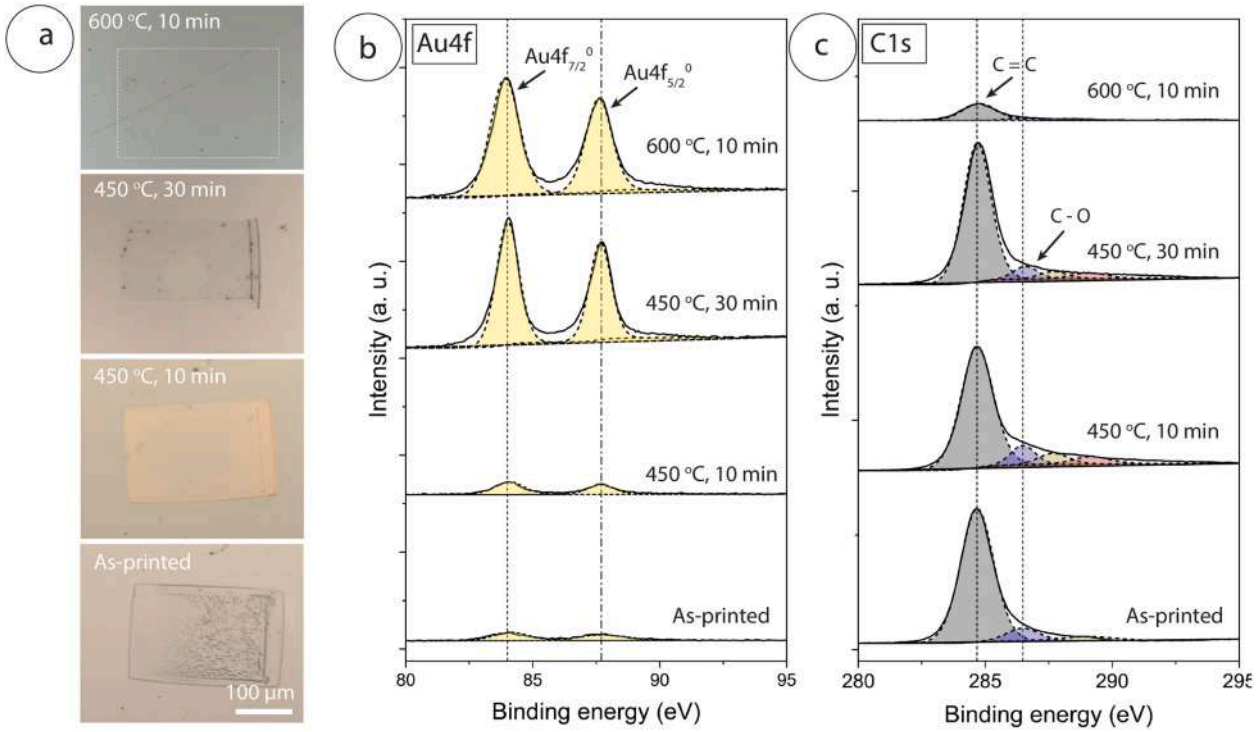

Fig. 3. (a) Optical microscopic images of large area 2D patterns of organometallic ice, both as printed and post-processed with various annealing parameters. The Au4f and C1s signals were also compared for the patterns in (b) and (c).

differences. E.g. for FEBID, post-annealing in air and O_2 plasma treatments can increase metal content, producing higher purity and conductivity for Au-containing geometries. However, C cannot be completely removed [44,56]. In contrast, our study revealed through XPS that C vanished from 2DIL thin films after exposition to O_2 plasma. The XPS signals of Au correlate with a previous FEBID study [62], where reduced $Au4f_{7/2}$ signals are observed at 84.0 eV for $Au(acac)Me_2$ precursor irradiated by electrons on amorphous carbon and silver substrates. In 2PP, oxygen treatments remove carbonaceous residues from the prints' surface to enhance material properties and result in drastic

material loss [63].

3.3. Post-processing of 3D structures

To test our second hypothesis, that 3DIL materials resemble thermoset polymers, we thermally annealed 3D organometallic structures. Fig. 4 shows Benchy boats as printed and post-processed with Ar annealing at different temperatures for 10 min. SEM and optical microscopic images show the morphological changes.

The as-printed structures have dimensions of 40.4 μm and 31.3 μm in length and 14.3 μm and 10.7 μm in height, respectively (Fig. 4a). Annealing at 450 °C does not cause noticeable changes under SEM compared with the as-printed boats. Similar to Fig. 3a, a "goldish" color is visible with optical microscopy (Fig. 4b). We did not observe the drastic material loss seen earlier with the 2D patterns. This may be due to the larger surface area of the 2D layer compared with 3D objects. At 600 °C, the bottom layers of the structures started to vanish (red arrow in Fig. 4c), along with the corners (green arrow in Fig. 4c). This morphological change is also apparent under optical microscopy, showing dark surfaces with high optical absorption. At 800 °C, we observed a significant material loss, and the entire structures started to detach from the Si substrate, as highlighted by the blue arrows in Fig. 4d.

We performed and compared EDS mapping in Fig. 4. Ar annealing significantly reduced O signals, especially at a high annealing temperature of 800 °C. However, we did not observe significant changes in the intensity of C and Au signals. This analysis provides important information regarding the parameter window for thermal annealing of 3D organometallic structures created by 3DIL.

We did not observe any melting evidence with material removal at elevated temperatures. Together with the above 2D annealing studies, our results show that 3DIL processed AuDa have thermoset properties because thermosets do not melt and directly decompose at higher temperatures. In contrast to organometallic FEBID devices, elevated temperatures (higher than 400 ℃) can induce void formation and shape distortion due to a large volume loss of C [56]. This is because they are nanocomposite materials formed by an amorphous carbon matrix with scattered metal [64]. In 2PP, photopolymers cross-link to form thermosets and decompose in the range of 400–450 ℃ [65], and our studies suggest IL-processed AuDa is more temperature-stable than 2PP materials.

3.4. Free metal mobility during post-processing

To test our final hypothesis, we created different patterns of organometallic ice on a TEM grid for TEM inspection. Fig. 5a shows a rectangular pattern (labeled by the white dash box) in the center of a TEM grid, which is composed of spiral-shaped metallic heaters and a Si_3N_4 film (in green color). There are a group of openings on the Si_3N_4 film, and TEM inspection was performed at the edge of these windows. Fig. 5b shows an SEM image of lines and dots printed close to the window edge, the resolution of the printed structures is around 2 μm. Fig. 5c shows the Si_3N_4 window on the TEM grid, where the printed rectangular film is located and extends over the edge. After the annealing process in a vacuum at 450 °C, we observed AuNPs scattered in the cross-linked AuDA thin film (indicated by the yellow arrows). A high-resolution TEM image (Fig. 5d) reveals well-resolved Au (111) (d = 0.24 nm) and Au (200) (d = 0.20 nm) crystalline lattices on a single AuNP with a diameter of around 10 nm. Similar results were also achieved for samples printed with lines and dots. These TEM findings are coherent with our observations of metallic colors (Figs. 3a and 4b), because the "shiny" metallic color is associated with a high optical reflection coefficient, which is caused by the interaction of light with free electrons in metals [66,67]. However, we did not expect electrical conduction due to the large distances between the Au nanoparticles. Micro four-point probe (M4PP) [68,69] conductivity measurements confirmed the insulative property of shiny thin films.

These findings confirm our third hypothesis that mobile Au atoms diffuse to form clusters. This is similar to 2PP, where elevated temperatures permit the diffusion of mobile metals, enabling the fabrication of AuNPs-containing devices. These 2PP devices target applications such as photonics, nanoplasmonics, or drug delivery [52,70]. FEBID can also produce nanoparticles that through post-growth thermal annealing serve for growing sites of nanostructures, such as carbon nanotubes [71]. But to our knowledge, FEBID gold nanoparticles have not been reported yet.

In summary, our work reveals the influence of different post-processing methods on 3DIL objects: uncovering their thermoset properties and the ability of mobile metal atoms to form clusters. Additionally, we presented ligand removal using oxygen-based post-processing.

4. Conclusions

This work is a pioneering investigation of 3DIL and post-processing methods using metalorganic precursors. We have demonstrated that (i) 3D objects can be created by 3DIL with Au(acac)Me_2 precursor; (ii) printed 3D objects can be purified with different post-processing methods, including O_2 plasma treatment, Ar annealing, and air annealing; (iii) Ar annealing at 600 °C can achieve a high purification effect for Au but with a significant material removal; (iv) Printed 3D objects exhibit thermoset property; (v) AuNPs can be created under thermal annealing process. These findings supported our three hypotheses. Firstly, oxygen-based treatments can remove carbon-based ligands while leaving noble metals behind. Secondly, 3DIL with AuDA is an effective method for fabricating submicrometer structures that behave like thermosets, which exhibit distinct mechanical properties and thermal stability compared to thermoplastics [72]. Lastly, mobile metals will

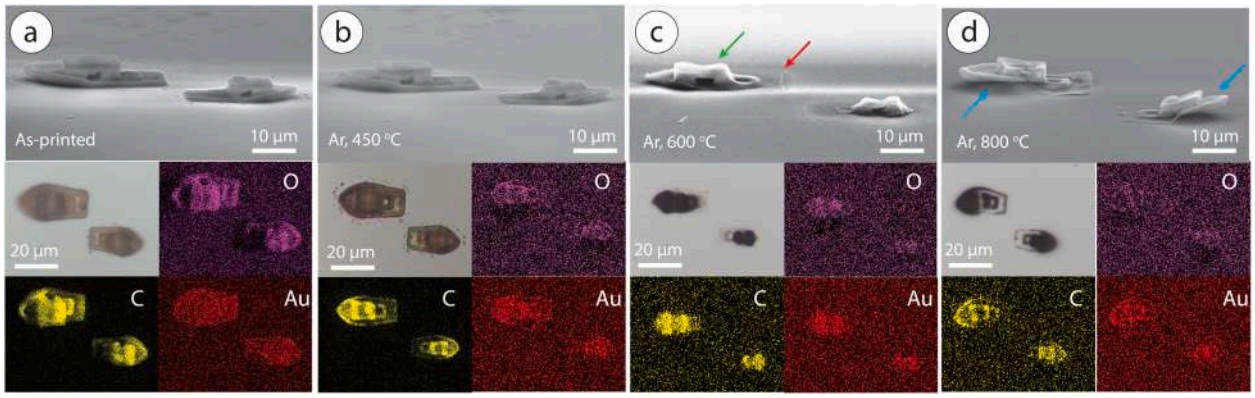

Fig. 4. Post-processing of Benchy structures with Ar annealing. SEM images, optical microscopic images, and EDS mapping are compared: (a) as printed. (b) 450 °C for 10 min. (c) 600 °C for 10 min. (d) 800 °C for 10 min.

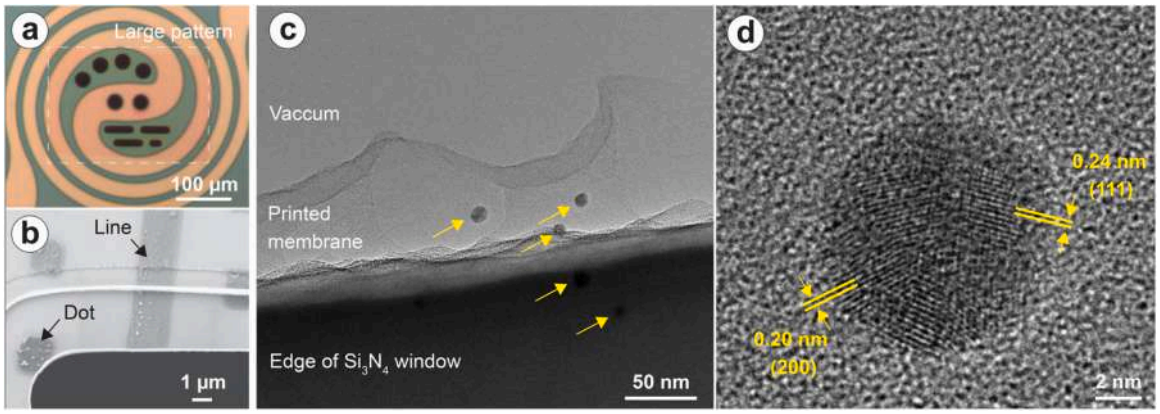

Fig. 5. TEM experiments with IL patterns. (a) Optical microscopic image showing a large pattern (in white dash box) printed at the center of a TEM grid. (b) SEM image showing dot and line patterns close to the edge of Si_3N_4 window. (c) TEM image of AuNPs (indicated by yellow arrows). (b) Lattice fringes of a polycrystalline AuNP.

diffuse at elevated temperatures to form AuNPs. The capabilities of organometallic compounds to detect environmental changes can position 3DIL for applications such as cancer or cardiovascular disease detection and gas sensing (environmental detection) [73,74]. We also infer that 3DIL processing of aromatic precursor might yield quantum dots [75] for quantum devices. Besides, High-density data storage was also reported [76] for 2DIL, and 3DIL could further increase data density. Similarly, 2D perovskite research [77] could be translated into high-efficiency mixed dimensional 2D-3D perovskite structures for optoelectronics applications [78,79]. Lastly, 3DIL can be used to manufacture AuNPs, which can be applied for drug delivery [52,70], biomedicine [80], biology [81] and catalysis [82]. Our study paves the way for further research on electron beam processing of metalorganic materials and post-processing, expanding the list of 3DIL materials and potential applications.

CRediT authorship contribution statement

Anpan Han: Writing – review & editing, Visualization, Validation, Supervision, Resources, Project administration, Methodology, Investigation, Funding acquisition, Formal analysis, Conceptualization. **Bingdong Chang:** Writing – review & editing, Writing – original draft, Visualization, Validation, Methodology, Investigation, Formal analysis. **Gwendoline A. E. Anand:** Writing – review & editing, Writing – original draft, Investigation, Formal analysis, Conceptualization. **Hoà Lê Thanh:** Writing – review & editing, Validation, Methodology, Investigation, Formal analysis, Data curation, Conceptualization. **Xiyuan Liu:** Writing – review & editing. **Thomas Willum Hansen:** Writing – review & editing, Validation, Methodology, Investigation, Formal analysis, Data curation. **Jose María De Teresa:** Writing – review & editing.

Declaration of Competing Interest

The authors declare the following financial interests/personal relationships which may be considered as potential competing interests: Anpan Han reports financial support was provided by Lundbeck Foundation. Bingdong Chang reports financial support was provided by Lundbeck Foundation. Anpan Han reports financial support was provided by Novo Nordisk Foundation. Anpan Han reports financial support was provided by Marie and M B Richter's Fund. If there are other authors, they declare that they have no known competing financial interests or personal relationships that could have appeared to influence the work reported in this paper.

Acknowledgments

We thank Spectral AB Sweden, the DTU Construct workshop, and DTU Nanolab for technical support.

We extend our gratitude to Daryl W. Yee for his meticulous proofreading and invaluable insights, which greatly enhanced the quality of this work. We also thank Carl Emil Andersen for his essential technical assistance with equipment handling. We thank Marcel A. J. Somers for his insightful input on XPS analysis. We thank Alice Bastos da Silva Fanta, Jonas Michael-Lindhard, and Mette Balslev for help with M4PP measurements. We thank Thomas Lundin Christiansen and Matteo Villa for the help with thermal annealing experiments.

Lundbeck Foundation grant R305–2018–2779 (AH)

Lundbeck Foundation grant R402–2022–1530 (BC)

Novo Nordisk Foundation grant NNF0064289 (AH)

Marie and B. Richters Foundation (AH)

MCIN/AEI/10.13039/ 501100011033 grant PID2020–112914RB-I00 (JMDT)

Gobierno de Aragón grant E13_23R (JMDT)

AI usage declaration.

During the preparation of this work the authors used Grammarly and ChatGPT in order to improve English. After using this tool/service, the authors reviewed and edited the content as needed and take full responsibility for the content of the publication.

Appendix A. Supporting information

Supplementary data associated with this article can be found in the online version at doi:10.1016/j.addma.2025.104645.

Data availability

Data will be made available on request.

References

[1] D. Li, J. He, Z. Song, K. Yao, M. Wu, H. Fu, Y. Liu, Z. Gao, J. Zhou, L. Wei, Z. Zhang, Y. Dai, Z. Xie, X. Yu, Miniaturization of mechanical actuators in skin-integrated electronics for haptic interfaces, Microsyst. Nanoeng. 7 (2021) 85, https://doi.org/10.1038/s41378-021-00301-x.

[2] B. Hertweck, Flat enameled micro wire drives miniaturization of electronics, ATZelectron. World 14 (2019) 56–58, https://doi.org/10.1007/s38314-019-0074-9.

[3] O. Ilchenko, Y. Pilhun, A. Kutsyk, D. Slobodianiuk, Y. Goksel, E. Dumont, L. Vaut, C. Mazzoni, L. Morelli, S. Boisen, K. Stergiou, Y. Aulin, T. Rindzevicius, T. E. Andersen, M. Lassen, H. Mundhada, C.B. Jendresen, P.A. Philipsen, M. Hædersdal, A. Boisen, Optics miniaturization strategy for demanding Raman spectroscopy applications, Nat. Commun. 15 (2024) 3049, https://doi.org/10.1038/s41467-024-47044-7.

[4] Y. Zang, Y. Zhu, W. Xie, Y. Yang, L. Bu, X. Liu, A bi-dimensional compressed Luneburg lens antenna for miniaturization based on transformation optics, Front. Phys. 10 (2022) 1–11, https://doi.org/10.3389/fphy.2022.1012470.

[5] R.Z. Gao, C.L. Ren, Synergizing microfluidics with soft robotics: a perspective on miniaturization and future directions, Biomicrofluidics 15 (2021), https://doi.org/10.1063/5.0036991.

[6] N. Thakur, T.R. Das, S. Patra, M. Choudhary, S.K. Shukla, Miniaturization devices: A nanotechnological approach, Electrochem. Sens. (2022) 241–259, https://doi.org/10.1016/B978-0-12-823148-7.00009-X. Elsevier.

[7] C.M. Krishna*, P.J. Vijay, P.S. Sai, D. Mounkeswari, Miniaturization of strips loaded hexagonal microstrip patch antenna for advanced communication, Int. J. Innov. Technol. Explor. Eng. 8 (2019) 2753–2757, https://doi.org/10.35940/ijitee.L2561.1081219.

[8] D. Gao, T. Li, Z. Bai, R. Ma, Z. Xie, S. Jia, W. Wang, X. Xie, Multi-modulation compatible miniaturization system for FSO communication assisted by chirp-managed laser, Opt. Express 30 (2022) 32306, https://doi.org/10.1364/OE.465160.

[9] S. Maruo, Stereolithography and Two-Photon Polymerization, Handb. Laser Micro-Nano-Eng. 2 (2021) 1375–1400, https://doi.org/10.1007/978-3-030-63647-0_24.

[10] M. Carlotti, V. Mattoli, Functional materials for two-photon polymerization in microfabrication, Small 15 (2019), https://doi.org/10.1002/smll.201902687.

[11] E. Fakeih, A.A. Aguirre-Pablo, S.T. Thoroddsen, K.N. Salama, Fabrication and characterization of porous microneedles for enhanced fluid injection and suction: a two-photon polymerization approach, Adv. Eng. Mater. 25 (2023) 1–8, https://doi.org/10.1002/adem.202300161.

[12] X. Wang, Z. Wei, C.Z. Baysah, M. Zheng, J. Xing, Biomaterial-based microstructures fabricated by two-photon polymerization microfabrication technology, RSC Adv. 9 (2019) 34472–34480, https://doi.org/10.1039/c9ra05645a.

[13] M. Lebedevaite, J. Ostrauskaite, E. Skliutas, M. Malinauskas, Photoinitiator free resins composed of plant-derived monomers for the optical μ-3D printing of thermosets, Polymers 11 (2019), https://doi.org/10.3390/polym11010116.

[14] S.K. Saha, D. Wang, V.H. Nguyen, Y. Chang, J.S. Oakdale, S.C. Chen, Scalable submicrometer additive manufacturing, Science 366 (80-.) (2019) 105–109, https://doi.org/10.1126/science.aax8760.

[15] B.H. Cumpston, S.P. Ananthavel, S. Barlow, D.L. Dyer, J.E. Ehrlich, L.L. Erskine, A. A. Heikal, S.M. Kuebler, I.-Y.S. Lee, D. McCord-Maughon, J. Qin, H. Röckel, M. Rumi, X. Wu, S.R. Marder, J.W. Perry, Two-photon polymerization initiators for three-dimensional optical data storage and microfabrication, Nature 398 (1999) 51–54, https://doi.org/10.1038/17989.

[16] H. Wang, W. Zhang, D. Ladika, H. Yu, D. Gailevičius, H. Wang, C. Pan, P.N.S. Nair, Y. Ke, T. Mori, J.Y.E. Chan, Q. Ruan, M. Farsari, M. Malinauskas, S. Juodkazis, M. Gu, J.K.W. Yang, Two-photon polymerization lithography for optics and photonics: fundamentals, materials, technologies, and applications, Adv. Funct. Mater. 33 (2023), https://doi.org/10.1002/adfm.202214211.

[17] B.R. Jany, K. Madajska, A. Butrymowicz-Kubiak, F. Krok, I.B. Szymańska, Pathway for unraveling chemical composition effects of metal-organic precursors for FIBID applications, Condens. Matter (2024), https://doi.org/10.48550/arXiv.2406.10022.

[18] I. Utke, P. Swiderek, K. Höflich, K. Madajska, J. Jurczyk, P. Martinović, I. B. Szymańska, Coordination and organometallic precursors of group 10 and 11: Focused electron beam induced deposition of metals and insight gained from chemical vapour deposition, atomic layer deposition, and fundamental surface and gas phase studies, Coord. Chem. Rev. 458 (2022), https://doi.org/10.1016/j.ccr.2021.213851.

[19] N. Marcano, S. Sangiao, M. Plaza, L. Prez, A.F. Pacheco, R. Córdoba, M.C. Sánchez, L. Morellón, M.R. Ibarra, J.M. De Teresa, Weak-antilocalization signatures in the magnetotransport properties of individual electrodeposited Bi Nanowires, Appl. Phys. Lett. 96 (2010) 1–4, https://doi.org/10.1063/1.3328101.

[20] K. Gross, J.J.P. Barragán, S. Sangiao, J.M. De Teresa, L. Lajaunie, R. Arenal, H. A. Calderón, P. Prieto, Electrical conductivity of oxidized-graphenic nanoplatelets obtained from bamboo: effect of the oxygen content, Nanotechnology 27 (2016), https://doi.org/10.1088/0957-4484/27/36/365708.

[21] H. Plank, R. Winkler, C.H. Schwalb, J. Hütner, J.D. Fowlkes, P.D. Rack, I. Utke, M. Huth, Focused electron beam-based 3D nanoprinting for scanning probe microscopy: a review, Micromachines 11 (2020), https://doi.org/10.3390/mi11010048.

[22] F.I. Allen, J.M. De Teresa, B. Onoa, Focused helium ion and electron beam-induced deposition of organometallic tips for dynamic atomic force microscopy of biomolecules in liquid, ACS Appl. Mater. Interfaces 16 (2024) 4439–4448, https://doi.org/10.1021/acsami.3c16407.

[23] F. Sigloch, S. Sangiao, P. Orús, J.M. de Teresa, Direct-write of tungsten-carbide nanoSQUIDs based on focused ion beam induced deposition, Nanoscale Adv. 4 (2022) 4628–4634, https://doi.org/10.1039/d2na00602b.

[24] F. Porrati, F. Jungwirth, S. Barth, G.C. Gazzadi, S. Frabboni, O.V. Dobrovolskiy, M. Huth, Highly-packed proximity-coupled DC-Josephson junction arrays by a direct-write approach, Adv. Funct. Mater. 32 (2022), https://doi.org/10.1002/adfm.202203889.

[25] L. Serrano-Ramón, R. Córdoba, L.A. Rodríguez, C. Magén, E. Snoeck, C. Gatel, I. Serrano, M.R. Ibarra, J.M. De Teresa, Ultrasmall functional ferromagnetic nanostructures grown by focused electron-beam-induced deposition, ACS Nano 5 (2011) 7781–7787, https://doi.org/10.1021/nn201517r.

[26] C. Donnelly, A. Hierro-Rodríguez, C. Abert, K. Witte, L. Skoric, D. Sanz-Hernández, S. Finizio, F. Meng, S. McVitie, J. Raabe, D. Suess, R. Cowburn, A. Fernández-Pacheco, Complex free-space magnetic field textures induced by three-dimensional magnetic nanostructures, Nat. Nanotechnol. 17 (2022) 136–142, https://doi.org/10.1038/s41565-021-01027-7.

[27] M. Esposito, V. Tasco, F. Todisco, M. Cuscunà, A. Benedetti, D. Sanvitto, A. Passaseo, Triple-helical nanowires by tomographic rotatory growth for chiral photonics, Nat. Commun. 6 (2015) 1–7, https://doi.org/10.1038/ncomms7484.

[28] R. Winkler, F. Schmidt, U. Haselmann, J.D. Fowlkes, B.B. Lewis, G. Kothleitner, P. D. Rack, H. Plank, Direct-write 3D nanoprinting of plasmonic structures, Appl. Mater. Interfaces 9 (2017) 8233–8240, https://doi.org/10.1021/acsami.6b13062.

[29] P. Bøggild, T.M. Hansen, C. Tanasa, F. Grey, Fabrication and actuation of customized nanotweezers with a 25 nm gap, Nanotechnology 12 (2001) 331–335, https://doi.org/10.1088/0957-4484/12/3/322.

[30] A.K. Waafi, B. Chang, J. Lyngholm- Kjærby, R.I. Haque, A. Han, Electron beam processing of organic ice for low-toxicity submicrometer additive manufacturing, Addit. Manuf. 84 (2024) 104114, https://doi.org/10.1016/j.addma.2024.104114.

[31] A. Elsukova, A. Han, D. Zhao, M. Beleggia, Effect of molecular weight on the feature size in organic ice resists, Nano Lett. 18 (2018) 7576–7582, https://doi.org/10.1021/acs.nanolett.8b03130.

[32] D.W. Yee, M.L. Lifson, B.W. Edwards, J.R. Greer, Additive manufacturing of 3D-architected multifunctional metal oxides, Adv. Mater. 31 (2019), https://doi.org/10.1002/adma.201901345.

[33] A. Vyatskikh, S. Delalande, A. Kudo, X. Zhang, C.M. Portela, J.R. Greer, Additive manufacturing of 3D nano-architected metals, Nat. Commun. 9 (2018), https://doi.org/10.1038/s41467-018-03071-9.

[34] M.A. Saccone, R.A. Gallivan, K. Narita, D.W. Yee, J.R. Greer, Additive manufacturing of micro-architected metals via hydrogel infusion, Nature 612 (2022) 685–690, https://doi.org/10.1038/s41586-022-05433-2.

[35] A.V. Riazanova, Y.G.M. Rikers, J.J.L. Mulders, L.M. Belova, Pattern shape control for heat treatment purification of electron-beam-induced deposition of gold from the Me 2Au(acac) precursor, Langmuir 28 (2012) 6185–6191, https://doi.org/10.1021/la203599c.

[36] J. Pablo-Navarro, C. Magén, J.M. De Teresa, Purified and crystalline three-dimensional electron-beam-induced deposits: the successful case of cobalt for high-performance magnetic nanowires, ACS Appl. Nano Mater. 1 (2018) 38–46, https://doi.org/10.1021/acsanm.7b00016.

[37] C. Haverkamp, K. Höflich, S. Jäckle, A. Manzoni, S. Christiansen, Plasmonic gold helices for the visible range fabricated by oxygen plasma purification of electron beam induced deposits, Nanotechnology 28 (2017) 055303, https://doi.org/10.1088/1361-6528/28/5/055303.

[38] E. Begun, O.V. Dobrovolskiy, M. Kompaniiets, R. Sachser, C. Gspan, H. Plank, M. Huth, Post-growth purification of Co nanostructures prepared by focused electron beam induced deposition, Nanotechnology 26 (2015), https://doi.org/10.1088/0957-4484/26/7/075301.

[39] D. Belić, M.M. Shawrav, M. Gavagnin, M. Stöger-Pollach, H.D. Wanzenboeck, E. Bertagnolli, Direct-write deposition and focused-electron-beam-induced purification of gold nanostructures, ACS Appl. Mater. Interfaces 7 (2015) 2467–2479, https://doi.org/10.1021/am507327y.

[40] F. Porrati, L. Keller, C. Gspan, H. Plank, M. Huth, Electrical transport properties of Ga irradiated W-based granular nanostructures, J. Phys. D. Appl. Phys. 50 (2017), https://doi.org/10.1088/1361-6463/aa6bdb.

[41] R.I. Haque, A.K. Waafi, B. Chang, A. Han, Ice lithography using tungsten hexacarbonyl, Micro Nano Eng. 18 (2023) 100171, https://doi.org/10.1016/j.mne.2023.100171.

[42] R.I. Haque, A.K. Waafi, K. Jaemin, D. Briand, A. Han, 80 K cryogenic stage for ice lithography, Micro Nano Eng. 14 (2022) 100101, https://doi.org/10.1016/j.mne.2021.100101.

[43] W. Tiddi, A. Elsukova, H.T. Le, P. Liu, M. Beleggia, A. Han, Organic ice resists, Nano Lett. 17 (2017) 7886–7891, https://doi.org/10.1021/acs.nanolett.7b04190.

[44] D. Belic, M.M. Shawrav, E. Bertagnolli, H.D. Wanzenboeck, Direct writing of gold nanostructures with an electron beam: On the way to pure nanostructures by combining optimized deposition with oxygen-plasma treatment, Beilstein J. Nanotechnol. 8 (2017) 2530–2543, https://doi.org/10.3762/bjnano.8.253.

[45] O. Guise, H. Marbach, J. Levy, J. Ahner, J.T. Yates, Electron-beam-induced deposition of carbon films on Si(100) using chemisorbed ethylene as a precursor molecule, Surf. Sci. 571 (2004) 128–138, https://doi.org/10.1016/j.susc.2004.07.053.

[46] D. Belić, M.M. Shawrav, M. Gavagnin, M. Stöger-Pollach, H.D. Wanzenboeck, E. Bertagnolli, Direct-write deposition and focused-electron-beam-induced purification of gold nanostructures, ACS Appl. Mater. Interfaces 7 (2015) 2467–2479, https://doi.org/10.1021/am507327y.

[47] R. Winkler, J.D. Fowlkes, P.D. Rack, G. Kothleitner, H. Plank, Shape evolution and growth mechanisms of 3D-printed nanowires, Addit. Manuf. 46 (2021) 102076, https://doi.org/10.1016/j.addma.2021.102076.

[48] A.K. Waafi, B. Chang, J. Lyngholm- Kjærby, R.I. Haque, A. Han, Electron beam processing of organic ice for low-toxicity submicrometer additive manufacturing, Addit. Manuf. 84 (2024) 104114, https://doi.org/10.1016/j.addma.2024.104114.

[49] A. Weitzer, R. Winkler, D. Kuhness, G. Kothleitner, H. Plank, Controlled morphological bending of 3D-FEBID structures via electron beam curing, Nanomaterials 12 (2022), https://doi.org/10.3390/nano12234246.

[50] M. Huth, F. Porrati, S. Barth, Living up to its potential—direct-write nanofabrication with focused electron beams, J. Appl. Phys. 130 (2021), https://doi.org/10.1063/5.0064764.

[51] L.J. Jiang, J.H. Campbell, Y.F. Lu, T. Bernat, N. Petta, Direct writing target structures by two-photon polymerization, Fusion Sci. Technol. 70 (2016) 295–309, https://doi.org/10.13182/FST15-222.

[52] J. Im, Y. Liu, Q. Hu, G.F. Trindade, C. Parmenter, M. Fay, Y. He, D.J. Irvine, C. Tuck, R.D. Wildman, R. Hague, L. Turyanska, Strategies for integrating metal nanoparticles with two-photon polymerization process: toward high resolution

functional additive manufacturing, Adv. Funct. Mater. 33 (2023), https://doi.org/10.1002/adfm.202211920.
[53] J. Lasseter, P.D. Rack, S.J. Randolph, Selected area deposition of high purity gold for functional 3D architectures, Nanomaterials 13 (2023) 757, https://doi.org/10.3390/nano13040757.
[54] M.V.P. dos Santos, A. Szkudlarek, A. Rydosz, C. Guerra-Nuñez, F. Béron, K. R. Pirota, S. Moshkalev, J.A. Diniz, I. Utke, Comparative study of post-growth annealing of Cu(hfac)2, Co2(CO)8 and Me2Au(acac) metal precursors deposited by FEBID, Beilstein J. Nanotechnol. 9 (2018) 91–101, https://doi.org/10.3762/bjnano.9.11.
[55] D. Kuhness, A. Gruber, R. Winkler, J. Sattelkow, H. Fitzek, I. Letofsky-Papst, G. Kothleitner, H. Plank, High-fidelity 3D nanoprinting of plasmonic gold nanoantennas, ACS Appl. Mater. Interfaces 13 (2021) 1178–1191, https://doi.org/10.1021/acsami.0c17030.
[56] A. Botman, J.J.L. Mulders, C.W. Hagen, Creating pure nanostructures from electron-beam-induced deposition using purification techniques: a technology perspective, Nanotechnology 20 (2009) 372001, https://doi.org/10.1088/0957-4484/20/37/372001.
[57] T. Koch, W. Zhang, T.T. Tran, Y. Wang, A. Mikitisin, J. Puchhammer, J.R. Greer, A. Ovsianikov, F. Chalupa-Gantner, M. Lunzer, Approaching standardization: mechanical material testing of macroscopic two-photon polymerized specimens, Adv. Mater. 36 (2024), https://doi.org/10.1002/adma.202308497.
[58] A.J. Gross, K. Bertoldi, Additive manufacturing of nanostructures that are delicate, complex, and smaller than ever, Small 15 (2019) 1–6, https://doi.org/10.1002/smll.201902370.
[59] M. Todeschini, A. Bastos da Silva Fanta, F. Jensen, J.B. Wagner, A. Han, Influence of Ti and Cr adhesion layers on ultrathin Au films, ACS Appl. Mater. Interfaces 9 (2017) 37374–37385, https://doi.org/10.1021/acsami.7b10136.
[60] J.-P. Sylvestre, A.V. Kabashin, E. Sacher, M. Meunier, J.H.T. Luong, Nanoparticle size reduction during laser ablation in aqueous solutions of cyclodextrins, in: P.R. Herman, J. Fieret, A. Pique, T. Okada, F.G. Bachmann, W. Hoving, K. Washio, X. Xu, J.J. Dubowski, D.B. Geohegan, F. Traeger (Eds.), Phot. Process. Microelectron. Photonics III, 2004: p. 84. https://doi.org/10.1117/12.525499.
[61] K. Kwon, B.L. Suh, K. Park, J. Kim, H.-T. Jung, Ultra-dense (~20 Tdot/in2) nanoparticle array from an ordered supramolecular dendrimer containing a metal precursor, Sci. Rep. 9 (2019) 3885, https://doi.org/10.1038/s41598-019-40363-6.
[62] J.D. Wnuk, J.M. Gorham, S.G. Rosenberg, W.F. van Dorp, T.E. Madey, C.W. Hagen, D.H. J, Electron beam irradiation of dimethyl-(acetylacetonate) gold(III) adsorbed onto solid substrates, J. Appl. Phys. (2010), https://doi.org/10.1063/1.3295918.
[63] M. Power, A. Barbot, F. Seichepine, G.-Z. Yang, Bistable, Pneumatically actuated microgripper fabricated using two-photon polymerization and oxygen plasma etching, Adv. Intell. Syst. 5 (2023), https://doi.org/10.1002/aisy.202200121.
[64] S. Graells, R. Alcubilla, G. Badenes, R. Quidant, Growth of plasmonic gold nanostructures by electron beam induced deposition, Appl. Phys. Lett. 91 (2007) 1–4, https://doi.org/10.1063/1.2786600.
[65] M.I. Sharipova, T.G. Baluyan, K.A. Abrashitova, G.E. Kulagin, A.K. Petrov, A. S. Chizhov, T.B. Shatalova, D. Chubich, D.A. Kolymagin, A.G. Vitukhnovsky, V. O. Bessonov, A.A. Fedyanin, Effect of pyrolysis on microstructures made of various photoresists by two-photon polymerization: comparative study, Opt. Mater. Express 11 (2021) 371, https://doi.org/10.1364/ome.416457.
[66] M. Fox, Optical Properties of Solids, in: Oxford Master Ser., 2nd ed., 2010: pp. 180–185.
[67] A. Kristensen, J.K.W. Yang, S.I. Bozhevolnyi, S. Link, P. Nordlander, N.J. Halas, N. A. Mortensen, Plasmonic colour generation, Nat. Rev. Mater. 2 (2016), https://doi.org/10.1038/natrevmats.2016.88.
[68] A. Han, H.H. Henrichsen, A. Savenko, D.H. Petersen, O. Hansen, Towards diamond micro four-point probes, Micro Nano Eng. 5 (2019) 100037, https://doi.org/10.1016/j.mne.2019.05.002.
[69] D.H. Petersen, O. Hansen, T.M. Hansen, P. Bøggild, R. Lin, D. Kjær, P.F. Nielsen, T. Clarysse, W. Vandervorst, E. Rosseel, N.S. Bennett, N.E.B. Cowern, Review of electrical characterization of ultra-shallow junctions with micro four-point probes, J. Vac. Sci. Technol. B, Nanotechnol. Microelectron. Mater. Process. Meas. Phenom. 28 (2010) C1C27–C1C33, https://doi.org/10.1116/1.3224898.
[70] V. Tribuzi, D.S. Corrêa, W. Avansi, C. Ribeiro, E. Longo, C.R. Mendonça, Indirect doping of microstructures fabricated by two-photon polymerization with gold nanoparticles, Opt. Express 20 (2012) 21107, https://doi.org/10.1364/oe.20.021107.
[71] R. Sharma, E. Moore, P. Rez, M.M.J. Treacy, Site-specific fabrication of Fe particles for carbon nanotube growth, Nano Lett. 9 (2009) 689–694, https://doi.org/10.1021/nl803180e.
[72] B. Liu, M.M. Abu-Omar, Lignin extraction and valorization using heterogeneous transition metal catalysts, Adv. Inorg. Chem. (2021) 137–174, https://doi.org/10.1016/bs.adioch.2021.02.001.
[73] J. Zheng, J. Hao, F. Ling, H. Jing, Y. Chen, T. Zhou, L. Fang, Q. Chen, M. Zhou, Two-dimensional Au-1,3,5 triethynylbenzene organometallic lattice: structure, half-metallicity, and gas sensing, J. Chem. Phys. 149 (2018), https://doi.org/10.1063/1.5038655.
[74] D.P. Mishra, B. Acharya, S. Tripathy, B. Barik, P.K. Sahu, An overview of the biosensing potential of organometallic compounds, Chem. Phys. Impact 7 (2023) 100326, https://doi.org/10.1016/j.chphi.2023.100326.
[75] Y. Lu, B. Jin, R. Zheng, S. Wu, D. Zhao, M. Qiu, Production and patterning of fluorescent quantum dots by cryogenic electron-beam writing, ACS Appl. Mater. Interfaces 15 (2023) 12154–12160, https://doi.org/10.1021/acsami.2c21052.
[76] R. Zheng, D. Zhao, Y. Lu, S. Wu, G. Yao, D. Liu, M. Qiu, Recording messages on nonplanar objects by cryogenic electron-beam writing, Adv. Funct. Mater. 32 (2022), https://doi.org/10.1002/adfm.202112894.
[77] B. Jin, Y. Lu, J. Sun, X. Sun, L. Wen, Q. Zhang, D. Zhao, M. Qiu, Cryogenic electron-beam writing for perovskite metasurface, Nano Lett. 24 (2024), https://doi.org/10.1021/acs.nanolett.4c00954.
[78] E.B. Kim, M.S. Akhtar, H.S. Shin, S. Ameen, M.K. Nazeeruddin, A review on two-dimensional (2D) and 2D-3D multidimensional perovskite solar cells: perovskites structures, stability, and photovoltaic performances, J. Photochem. Photobiol. C. Photochem. Rev. 48 (2021) 100405, https://doi.org/10.1016/j.jphotochemrev.2021.100405.
[79] M.A. Mahmud, T. Duong, Y. Yin, H.T. Pham, D. Walter, J. Peng, Y. Wu, L. Li, H. Shen, N. Wu, N. Mozaffari, G. Andersson, K.R. Catchpole, K.J. Weber, T. P. White, Double-sided surface passivation of 3D perovskite film for high-efficiency mixed-dimensional perovskite solar cells, Adv. Funct. Mater. 30 (2020), https://doi.org/10.1002/adfm.201907962.
[80] E. Çakmakçi, POSS—Thermosetting polymer nanocomposites, in: Polyhedral Oligomeric Silsesquioxane Polym. Nanocomposites, Elsevier, 2021, pp. 127–175, https://doi.org/10.1016/B978-0-12-821347-6.00004-4.
[81] S. Najah Saud Al-Humairi, Introductory chapter: gold nanoparticles – scientific background and potential horizons, in: Gold Nanoparticles Their Appl. Eng., IntechOpen, 2023, https://doi.org/10.5772/intechopen.109368.
[82] B. Liu, J. Jin, B. Ran, C. Chen, J. Li, N. Qin, Y. Zhu, Continuous production of bimetallic nanoparticles on carbon nanotubes based on 3D-printed microfluidics, Nanoscale 16 (2024) 2565–2573, https://doi.org/10.1039/d3nr05090d.